ELSEVIER

Contents lists available at ScienceDirect

International Journal of Fatigue

journal homepage: www.elsevier.com/locate/ijfatigue





Microstructural statistics for low-cycle fatigue crack initiation in $\alpha+\beta$ titanium alloys: A microstructure based RVE assessment

C. Bean ^a, J.C. Stinville ^a, A. Naït-Ali ^b, Z. Wu ^c, F. Sun ^c, F. Prima ^c, S. Hémery ^{b,*}

- ^a Materials Science and Engineering, University of Illinois at Urbana-Champaign, USA
- b Institut Pprime, ISAE-ENSMA, Université de Poitiers, CNRS UPR CNRS 3346, ISAE-ENSMA, Téléport 2, 1 avenue Clément Ader, 86961 Futuroscope-Chasseneuil, France
- c PSL Research University, Chimie ParisTech, CNRS UMR 8347, Institut de Recherche de Chimie Paris, Paris 75005, France

ARTICLE INFO

Keywords: Ti-6Al-4V Titanium alloys Fatigue crack initiation Microstructural statistics Grain boundaries

ABSTRACT

(0001) twist grain boundaries (BTGB) have been identified as critical microstructure configurations regarding fatigue crack initiation in titanium alloys. In the presently reported study, Ti-Al-V based alloys with different microstructures were tested in the low-cycle fatigue regime. Early cracking occurred at BTGB for all investigated alloys and microstructures. Microstructural statistics collected at crack initiation sites revealed a weak sensitivity to moderate differences in α and β stabilizers content and microstructural features. Criteria for the identification of crack initiation sites were then defined using this dataset. An automatic processing routine was applied on large-scale electron back-scattered diffraction maps to analyze the spatial distribution of BTGB susceptible to cracking. The low associated density implies that large microstructural regions, i.e., typically $> 1 \text{ mm}^2$, must be considered to include microstructural configurations prone to crack nucleation. It is likely to play a critical role in the high lifetime variability of Ti alloys.

1. Introduction

The fatigue performance of titanium alloys is a critical property for aerospace applications. As components must withstand a number of flights, mechanical loadings experienced in service are generally cyclic. The high strength-to-weight ratio and fatigue resistance make titanium alloys attractive for such applications. However, numerous studies highlighted a significant lifetime variability in the high cycle fatigue regime [1-5]. The number of cycles to failure can typically vary by several orders of magnitude for a given loading condition. A transition from surface to internal crack initiation accompanies increased lifetimes, as also observed for decreasing peak stress values. This feature has been reported to occur typically around 10^6-10^7 cycles [2,6,7]. While this implies a change in crack initiation and growth environment, a substantial variability has been reported considering surface crack initiation only [2,3,5]. The analysis of microstructural configurations found at crack initiation sites suggests no change in mechanism. Crack initiation facets are parallel to basal planes and preferentially form in equiaxed α grains [6,8]. However, subtle differences in crystallographic orientations suggest that the weights of the shear and normal stress components are linked with the differences in lifetimes [2,3]. Therefore,

local and neighboring microstructural configurations must be considered for accurate fatigue life predictions [5,9,10]. Inherent microstructural heterogeneities led to a growing interest in approaches for upscaling from laboratory scale samples and simulated volume elements to components [11-13].

The identification of crack nucleation sites is then of utmost importance to improve lifetime predictions and design fatigue resistant materials. The characterization of microstructural configurations critical for fatigue crack initiation has been the focus of numerous research efforts. While some controversy still exists, seminal studies reported a crucial role of α grains experiencing a high resolved shear stress for basal slip and a high stress component normal to the basal plane [8,14–16]. Therefore, a high density of potential crack nucleation sites is expected. Lavogiez et al. recently observed early fatigue crack nucleation at basal twist grain boundaries (BTGB) separating equiaxed α grains in Ti-6Al-4V [17]. This observation was then generalized to numerous alloys with different microstructures and a wide range of loading conditions [6,18]. Other research groups reported crack formation at BTGB [19-21]. Microstructural configurations were characterized to define criteria for identifying potential crack initiation sites [6,17,18,22]. The density of BTGB is not well documented due to the prohibitive time-consuming

E-mail address: Samuel.hemery@ensma.fr (S. Hémery).

^{*} Corresponding author.

nature of manual identification processes. A prior study suggests that it is typically about a few BTGB per squared millimeter [6]. Such value implies a high number of crack initiation candidates at the scale of industrial components. However, laboratory-scale analyses generally involve millimeter-scale specimens, and smaller regions of interest are sometimes considered. This feature raises concerns about the representativity of extracted information. It echoes the high variability in fatigue lives, related to specific microstructural configurations leading to early crack nucleation [9]. The combined role of BTGB and their low density offers a possible clarification of the observed scatter and provides new insights into the consideration of statistically representative microstructural elements. Assessment of the size of representative volume elements (RVE) for fatigue crack initiation is critical to understand the origin of lifetime variability and guiding future studies focused on fatigue of Ti alloys.

Many research studies have focused on determining RVE sizes [23]. For example, thermal [24], elastic [24] and plastic or viscoplastic properties [25-27] were considered. RVE sizes for strength [28,29] and plastic deformation have been mainly investigated in titanium and its alloys [27,30,31]. A recent study highlighted the relationship between the fatigue strength and slip activity in various metals and alloys, including titanium [32]. However, RVE size assessment regarding fatigue properties [23,33], especially crack nucleation [34], was rarely achieved regardless of the material. The study of micromechanical fields such as slip activity and stress concentrations must be complemented by microstructural data to predict crack nucleation sites reliably. This feature was clearly illustrated by the difference in RVE size reported for slip activity and fatigue crack initiation [34], which results from the more critical role of the microstructure in fatigue crack initiation than in strength, for example [35]. While average values of microstructural features govern strength and strain hardening, extreme values of the statistical distribution of microstructural features trigger localized deformation and damage. However, limited data is available on critical features of BTGB to the best of the authors' knowledge, especially statistically meaningful datasets. As a comparison, twin boundary characterization and data analysis has been carried out in Ni-based superalloys in a RVE size assessment framework [34,36].

The outline of the work described in the present article is then defined as follows: i. microstructural statistics were first collected to highlight critical features of microstructural configurations being candidates to fatigue crack initiation, ii. a processing routine was developed to identify potential crack initiation sites using EBSD data, and iii. the RVE size for fatigue crack initiation was finally determined. For this purpose, microstructural statistics were obtained from low-cycle fatigue crack initiation sites in different alloys with various microstructures. Several Ti-Al-V alloys were considered to account for the consequences of differences in composition on BTGB cracking susceptibility. This approach enabled the definition of microstructural configurations candidates to crack initiation based on a statistically significant number of observations. Automated processing of EBSD maps was then developed to detect BTGB. The density of BTGB was then estimated in Ti-6Al-4V with an equiaxed microstructure and a shallow degree of microtexture, which constitutes a reference material. This BTGB detection tool was then used in combination with microstructural criteria to highlight crack nucleation candidates using a fully automated routine. From this, a procedure based on a convergence criterion was applied to estimate the RVE size regarding fatigue crack nucleation in the considered material. Consequences on the fatigue life variability are discussed alongside limitations inherent to the used procedure.

2. Material and experiments

2.1. Materials

Different Ti-Al-V based alloys were employed in the present study. Two Ti-6Al-4V (Ti-64) variants with different microstructures were

considered. Ti-6Al-4V with an equiaxed microstructure (Ti-64E) was used as a reference material [37]. The measured composition was Ti-6.3Al-4.1V-0.18Fe-0.18O. The material provided by the US Air Force was annealed at 950 °C for 2 h followed by cooling at a rate of 0.1 °C per minute before a final treatment at 700 $^{\circ}$ C for 2 h. The equiaxed α grain size is approximately 9 µm, and the associated surface area fraction is about 92 %. Ti-6Al-4V with a bi-modal microstructure (Ti-64BM) was also employed to highlight the influence of a lower area fraction of equiaxed α grains. This material was provided by Safran and is denoted as Ti-64BM in the following. The measured composition was Ti-6.5Al-4.2V-0.14Fe-0.21O. Thermo-mechanical history cannot be presently shared for confidentiality reasons. The primary α grain size is approximately 13 μm , and the associated surface area fraction is about 40 %. The remaining area fraction comprises lamellar α phase embedded in β phase. The lamella thickness is approximately 0.5 µm. Ti-5Al-4V (Ti-54), also sometimes referred to as Ti54M, and Ti-5Al-7.5V (Ti-575) were employed to highlight a possible influence of the composition on crack initiation mechanisms. In particular, the balance of α and β stabilizers differs while the main alloying elements are similar to Ti-64. The measured composition of Ti-54 was Ti-5.1Al-3.9V-0.8Mo-0.05Fe-0.17O. The material was annealed at 750 °C after thermo-mechanical processing in the $\alpha + \beta$ field. The resulting microstructure is almost fully equiaxed with a primary α grain size of about 9 µm, and an associated surface area fraction of about 76 %. The measured composition of Ti-575 was Ti-5.1Al-7.6V-0.3Si-0.54Fe-0.22O. The material was annealed at 850 °C for 1 h before a 8 h heat treatment at 500 °C. The resulting microstructure is bi-modal with a primary α grain size of about 5 μm and an associated surface area fraction of about 35 %. The average lamella thickness is about 0.2 µm. Micrographs showing the microstructures of the materials employed in this study are presented in Fig. 1.

2.2. Fatigue testing

Flat dogbone specimens were tested in the low-cycle fatigue regime. The gage length was 10 mm, the gage width was 2 mm, and the thickness was 1 mm. One face of each specimen was ground using SiC paper from 500 grade to 4000 grade prior to testing. A 9 μm diamond suspension was then used for a rough polishing before the final polishing step involving a mixture of 90% solution of colloidal silica containing 0.04 μm particles and 10 % hydrogen peroxide. This preparation procedure allows a mirror finish suitable for low surface residual stresses and EBSD measurements [6]. A trapezoidal loading waveform was applied using load control. An Instron 8862 MT universal testing machine was used for this purpose. Loading and unloading were achieved in 1 s, and minimum and maximum loads were held for 1 s. The maximum load was typically equivalent to 90 %-95 % of the yield strength, and the applied load ratio was 0.1. The fatigue test was stopped after a targeted number of cycles. One specimen was tested for Ti-64E, Ti-54 and Ti-575 materials. In contrast, two Ti-64BM specimens were tested until different numbers of cycles. The whole gage length of the specimen was observed using a Tescan Vega 3 scanning electron microscope (SEM) at an x1000 magnification. Back-scattered electrons (BSE) were collected for the efficient detection of microcracks.

2.3. EBSD characterization and detection of BTGB

EBSD datasets were collected using a Jeol 6100 SEM operated at 25 kV and equipped with a Hikari EBSD detector provided by EDAX. The beam current was approximately 2.5 nA. A 6 \times 6 binning was used to obtain 106 \times 80 pixels² patterns at 120 frames per second. Hexagonal steps were used with a spacing of 0.4 μm or smaller between measurement points. These characterization conditions allow an accurate description of the grain boundary geometry, as the average α grain size corresponds to more than 20 pixels while maintaining a reasonable acquisition time for large areas (i.e., in the millimeter range, as considered in the present study).

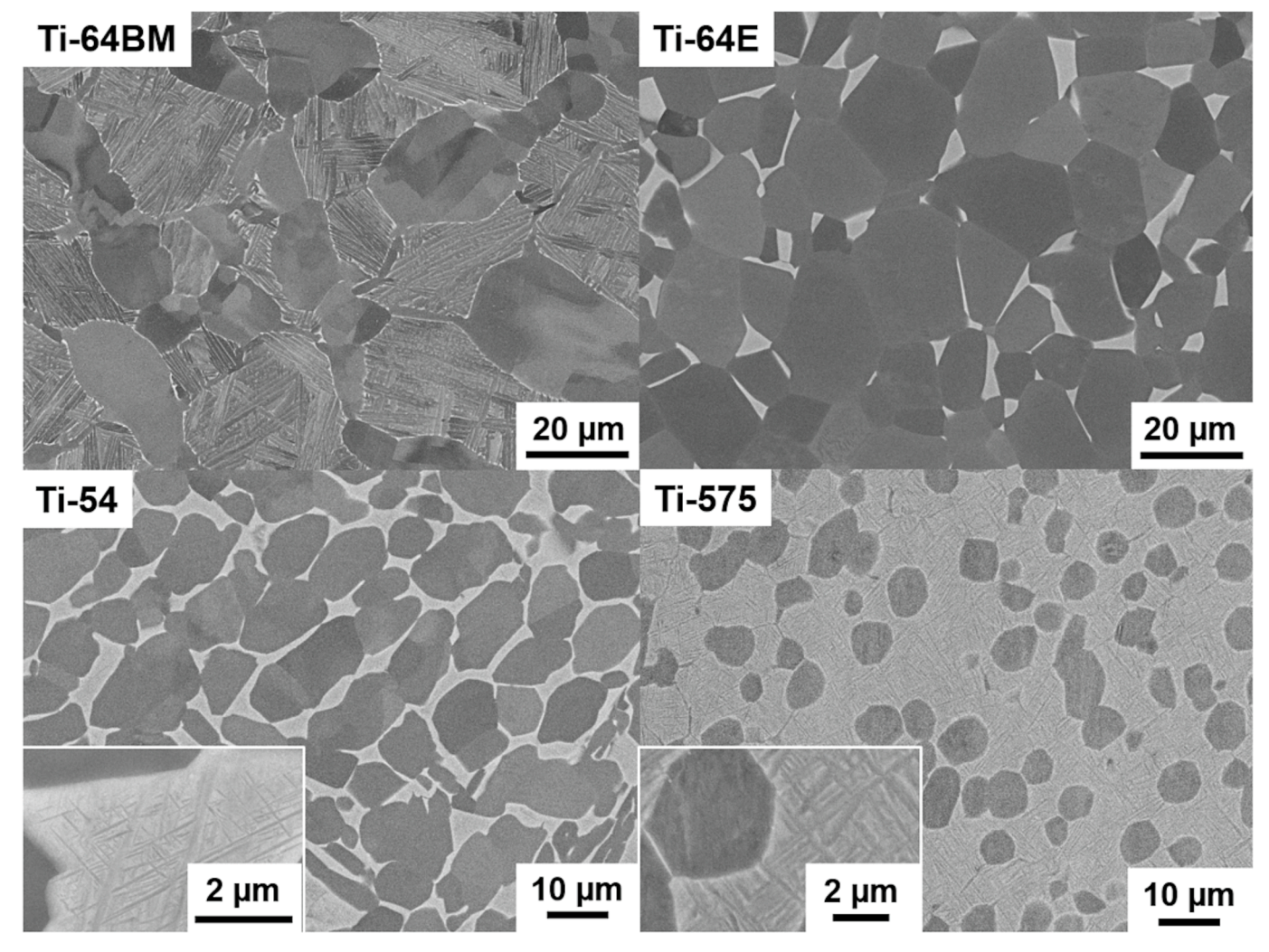


Fig. 1. Scanning electron microscopy micrographs showing the microstructures of the investigated materials. Back-scattered electrons show α phase in dark grey.

A new parameter was defined to identify BTGB in EBSD maps. Twist grain boundaries are defined by a crystallographic misorientation axis normal to the grain boundary plane, which corresponds to the (0001) plane for BTGB. Importantly, EBSD maps being collected on the surface of samples, the 3D geometry of the grain boundary is not known. Only the grain boundary trace can be used to identify BTGB. This is a significant source of uncertainty, which is further considered in the discussion section. The P parameter is proposed to assess the character of α/α grain boundaries. The equation is given below:

$$P = \alpha_1 \times \alpha_2 \tag{1}$$

With α_i the angle between the grain boundary trace and the c-axis of hexagonal close-packed (HCP) lattices in adjacent grains. Maximum values, which correspond to a perfect BTGB, are about 2.47 (i.e., $\frac{\pi^2}{4}$). The angles are schematically represented in Fig. 2. The Mtex toolbox for Matlab was employed to process EBSD maps [38]. P values were calculated for all α/α grain boundaries in the regions of interest.

2.4. Statistical analysis of the spatial distribution of potential crack initiation sites

A dedicated approach was employed to study the spatial distribution of BTGB and potential crack nucleation sites in the investigated material. A binary image was first generated from EBSD data processed to identify candidates for fatigue crack initiation. Matlab and Mtex were used for this purpose [38], before subsequent processing using an in-

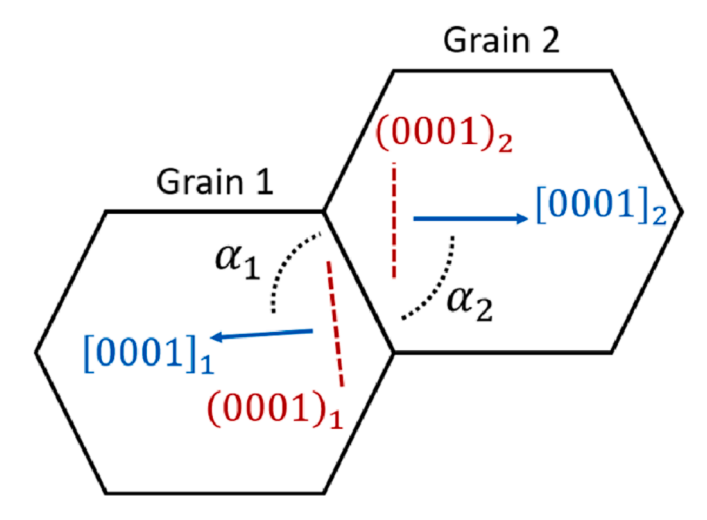


Fig. 2. Schematic representation of angles used to calculate P values.

house Python program. Random sampling was done by converting the image so that all the background had values of 0 and that each unique continuous region that defines a BTGB or a potential crack initiation site was labeled with a unique increasing integer to identify it as separate from the others. Then random sampling of the entire image was done at

increasing subset sizes N by N pixels with N starting at 0 pixels and increasing till 12,000 pixels with a step size of 25 pixels. For each subset size, 1000 random samples were taken, and the number of samples with at least 1 feature was calculated. The percentage of 1000 samples with at least 1 feature was finally determined.

3. Results

3.1. Statistics of crack initiation sites

Fatigue tests were carried out on the different materials. The yield stress, as defined using a 0.2 % plastic strain offset, and the ultimate tensile strength were assessed for all materials using a nominal strain rate of 10⁻² s⁻¹. The obtained values are reported in Table 1. The peak stress was set at 90 % of the 0.2 % proof stress except for Ti-575, which was applied at 95 %. The number of cycles was adjusted for each material to obtain a restricted number of microcracks, which ensures the detection of the most critical microstructure configurations. One specimen was tested for each material except Ti-64BM. Two tests were carried out and stopped after a different number of cycles to obtain additional information about the cracking susceptibility of different microstructural configurations. Information such as the peak stress, the number of cycles, and the cumulated plastic strain are reported in Table 1. A few cracks were found on the surface of each specimen. The number in each tested specimen is indicated in Table 1. All cracks were observed by SEM and characterized using EBSD. Typical examples are shown in Fig. 3. All cracks lie along straight grain boundaries parallel to the basal plane traces in adjacent grains. In addition, the misorientation is about the c-axes of the adjacent α grains, which are well aligned. These observations reveal the occurrence of BTGB cracking. Associated features are thoroughly detailed in the following paragraphs.

A variety of characteristics were extracted from the SEM and EBSD data for all cracks. The misalignment of c-axes of the HCP lattices was measured across all cracked grain boundaries. Three values were randomly picked along the crack to establish the distribution shown in Fig. 4a. 1° bins were used in this plot. The highest misalignment frequency corresponds to the interval from 0° to 1° . No value exceeded 4° . This shows that a very good alignment is needed for the grain boundaries to be candidates for crack initiation. In addition, measurements after crack opening are likely overestimating misalignment in the initial microstructure. However, the restricted length and the sharpness of the cracks suggest a limited contribution, which was about 1° in the example from [18]. The overall misorientation was also measured across the cracked grain boundaries. The distribution of the values is displayed in Fig. 4b using 5° bins. No specific rotation angle is associated with cracking. All values exceed 10° , and most belong to the $10^{\circ}-25^{\circ}$ range. No appreciable trend related to the alloy composition or microstructure could be extracted. This agrees well with conclusions from a prior study [18]. The overall distribution of values, which includes the present and previous datasets, is also shown in Fig. 4b and reveals a similar behavior. The cumulative distribution of the values is also shown in Fig. 4c to highlight more accurately the distribution of values. Less than 10 % of the values are lower than 10° or higher than 25°. Trends, including data from [18], overlap well with the distribution established in the present work. It shows an excellent statistical representativity of the considered

dataset.

The cracked BTGB length was measured for all cracks. Interestingly, the complete length of BTGBs was cracked, and no evidence of progressive crack growth was presently obtained. Values were divided by the average α grain size to lessen the influence of microstructure differences in considered materials. The distribution of the resulting values is shown in Fig. 4d. All values exceed 25 % of the grain size, and 90 % of the values exceed 40 % of the grain size. Interestingly, SEM characterization of the cracks revealed that low values are associated with the occurrence of slip transfer. Micrographs illustrating this feature are shown in Fig. 5. A low angle grain boundary favors this process, as shown in the EBSD map. Slip transfer may allow cracking on BTGB with a short segment connected to the specimen surface, artificially increasing the slip length. However, microcracks were generally arrested close to the end of the BTGB. This feature suggests that transgranular crack growth is more difficult than intergranular cracking along BTGB. Excluding cases associated with slip transmission, cracked BTGB segments are longer than 40 % of the average grain size. No meaningful trend was noticed as a function of the composition or the microstructure. No clear trend arose as well, considering the increase in the number of cycles, i.e., from 900 to 1800, applied to the Ti-64BM material. The cracked BTGB length was also measured using data from a prior study, and the distribution is indicated in Fig. 4d. The trends do overlap very well with data from the presently reported study. It suggests an excellent statistical representativity of the extracted trends.

Crystallographic orientations of all α grains separated by cracked BTGB are shown in Fig. 6a. The orientation is relative to the loading direction. A restricted orientation domain is concerned with BTGB cracking. This domain is generally associated with a high maximum Schmid factor for basal slip and a low misorientation between the c-axis of the HCP lattice and the loading direction [8,16,18]. The corresponding values are reported in Fig. 6b for each α grain. Misorientation values range between 15° and 65°, and maximum Schmid factors are higher than 0.25. It is worth noting that minimum and maximum angles, as well as the minimum Schmid factor values, are associated with the Ti-64BM specimen subjected to 1800 cycles. In contrast, cracks in the other Ti-64BM specimen, which were nucleated after a lower number of cycles (i.e., 900 cycles), belong to a more restricted range of values. In particular, misorientation angles are 33° and 43° for the Ti-64BM 900 specimen. Other Ti-64BM specimens were tested until 1 or 2 cracks formed in a prior study [18], and the maximum measured misorientation was 50° while it is 63° in the Ti-64BM specimen tested up to 1800 cycles, which led to the formation of 9 microcracks. This suggests that early cracks form for higher Schmid factors and intermediate misorientation values. Distribution of values in the same material was also reported by Lavogiez et al., with a higher number of microcracks N_{Cracks} (i.e., 45), which leads to a higher crack density than considered in this study. The associated crystallographic orientation domain is indicated with dashed lines in Fig. 5c. This dataset tends to confirm the extension of crystallographic orientation domains associated with the initiation of multiple cracks.

Values of the P parameter were calculated along the cracked BTGB. The limited crack opening ensures a moderate evolution from the grain boundary features due to cracking. Profiles of P values are plotted in Fig. 7 for all considered cracks. The profiles display micrometers-long

Table 1
Summary of details related to fatigue tested specimens including the material, the associated 0.2% proofs stress, the ultimate tensile strength, the peak stress magnitude, the number of cycles, the accumulated plastic strain, the number of cracks detected, and the number of cracks located at BTGB.

Material	0.2 % proof stress (MPa)	Ultimate tensile strength (MPa)	Peak stress (fraction of 0.2% proof stress)	Number of cycles before stop	Cumulated plastic strain	Number of surface cracks	Number of cracks at BTGB
Ti64E	919	938	90%	1000	0.0050	2	2
Ti64BM	998	1042	90%	1800	0.0039	9	9
Ti64BM	998	1042	90%	900	0.0029	2	2
Ti575	1199	1237	95%	2000	0.0131	3	3
Ti54	933	979	90%	1200	0.0100	5	5

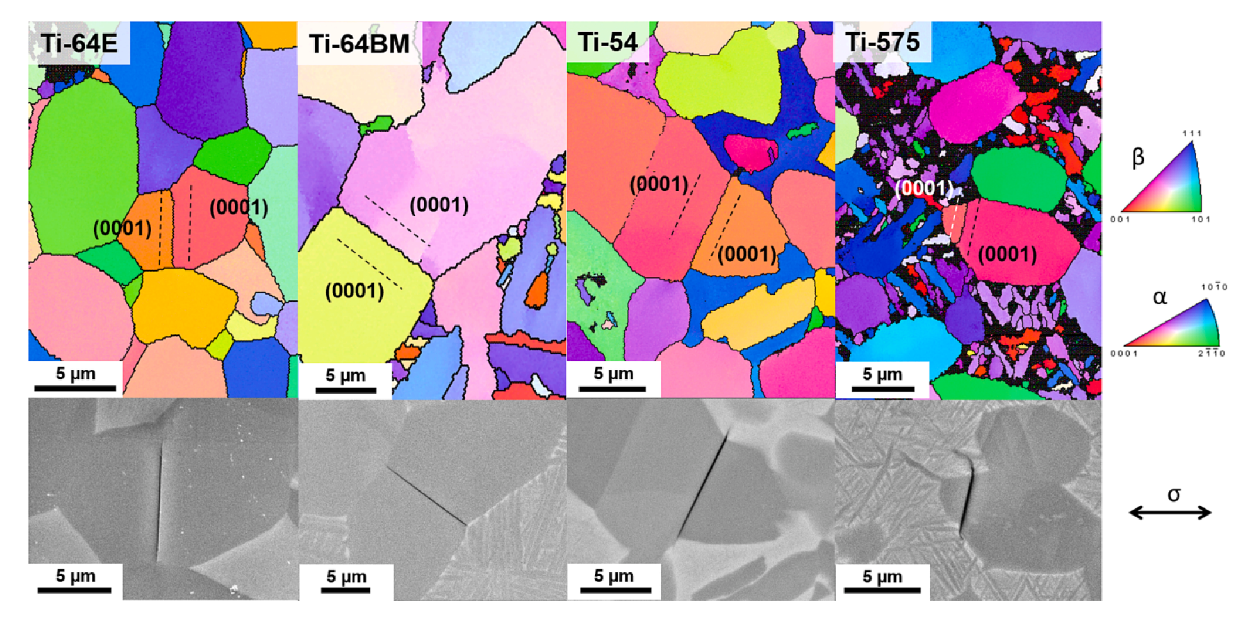


Fig. 3. Inverse pole figure maps showing the crystallographic orientations along the loading direction near a typical microcrack for each material. The surrounding microstructure is visible in associated SEM micrographs. The loading direction is horizontal.

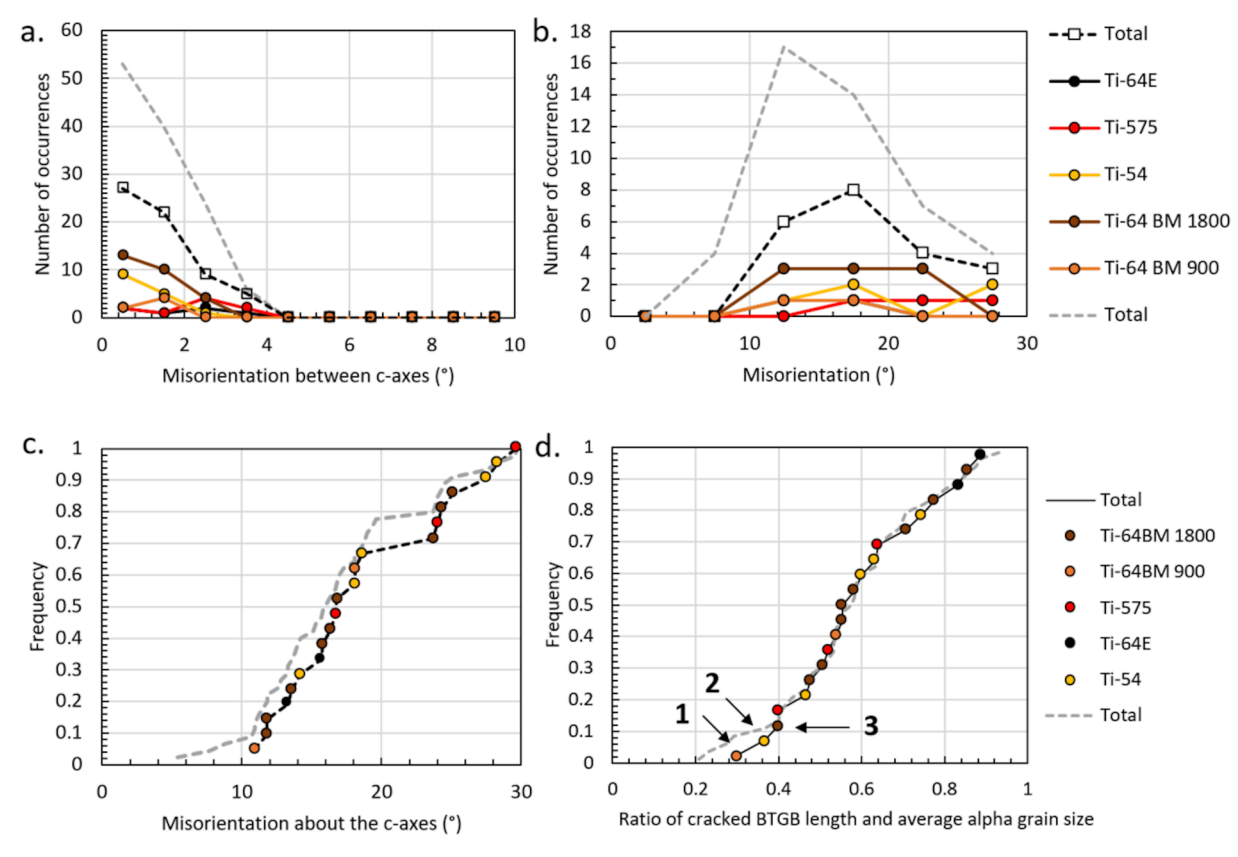


Fig. 4. a. Distributions of misorientation values measured between the c-axes of equiaxed α grains adjacent to cracked BTGB, b. Distributions of misorientation values measured between equiaxed α grains adjacent to cracked BTGB, c. The associated cumulative distribution plot and d. Cumulative distribution plot of cracked BTGB length. Light grey curves include data from [18]. Points numbered from 1 to 3 display short cracked BTGB segments.

segments reaching values higher than 2.25. Such a value is close to the 2.47 maximum value expected for pure twist character. The difference corresponds to a 4° deviation when both basal planes are equally misaligned and 8° when one plane trace is parallel while the other is misaligned. A binning step was applied to the Ti-64E dataset to investigate the effect of coarser step size (i.e., such as the one applied for mapping

large regions). Values were recalculated, and the corresponding profiles are reported with dashed lines in Fig. 7. No significant influence is observed.

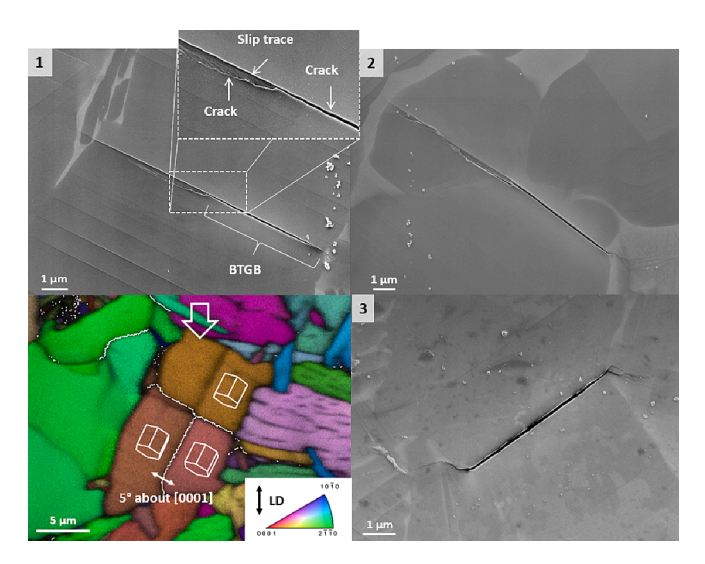


Fig. 5. Scanning electron microscopy micrographs showing cracks associated with short BTGB segments identified in Fig. 4d. Local crystallographic orientations in the region containing the crack number 1 is shown in a map of image quality superimposed with inverse pole figure colors coded along the loading direction (LD). The loading direction is vertical.

3.2. Detection of BTGB and fatigue crack nucleation sites

Due to the time and resources consuming nature of the collection of large EBSD maps, the following analysis of BTGB and RVE for crack initiation was carried out considering Ti64E only. This material was chosen as a baseline owing to a fully equiaxed microstructure and a low degree of microtexture [18]. A dedicated EBSD map of 3×5 mm² was collected with a hexagonal step of 0.4 μ m. 3 lines of 15 tiles were acquired. A total of approximately 140 million points were collected in

roughly 320 h. A single grain dilation cleanup step was applied to remove grains of less than 6 points with a misorientation threshold of 5° before processing to detect BTGB. P parameter values were calculated for all α/α grain boundaries contained in this region. Grain boundary segments with a length higher than 40 % of the average α grain size were considered to dismiss very short grain boundary segments, which are not candidates for crack initiation. It leads to a minimum of 8 pixels along a BTGB, satisfying the length criterion. All grain boundaries with a misorientation between c-axes higher than 4° or P values lower than 2.25 were ruled out of the analyses. A total of 117 grain boundary segments was found to meet these criteria. The resulting density is then about 7.8 mm $^{-2}$.

The distribution of misorientation values for all BTGB found in a 8 mm² region is shown in Fig. 8. The distributions for cracked BTGB found in the present and previous studies [18] are also displayed for comparison. Although the distributions do not perfectly overlap, trends are similar. For example, the maximum frequency is associated with the 10°-15° range. Furthermore, the frequency decreases for higher misorientation values. While cracked BTGB with misorientations lower than 10° were very rare, a fair amount of microstructural configurations were found. This might be related to the identification criteria, which implies a misorientation between c-axes lower than 4°, which is a loose criterion to identify BTGB when the grain boundary misorientation is of the same order of magnitude. Despite limitations in the BTGB identification procedure (e.g., bias due to crack opening, poor knowledge of the 3D grain boundary geometry), which can explain differences in values, similar trends suggest that the distribution of misorientation values for cracked BTGB reflects the features of existing BTGB population.

A fair amount of these BTGB are not candidates for crack initiation as they are not suitably oriented with respect to the loading axis to experience the required stress state. An additional criterion was then added regarding crystallographic orientations of α grains adjacent to BTGBs. Equiaxed α grains must exhibit a misorientation between the c-axis of the HCP lattice and the loading direction between 10° and 65° as well as

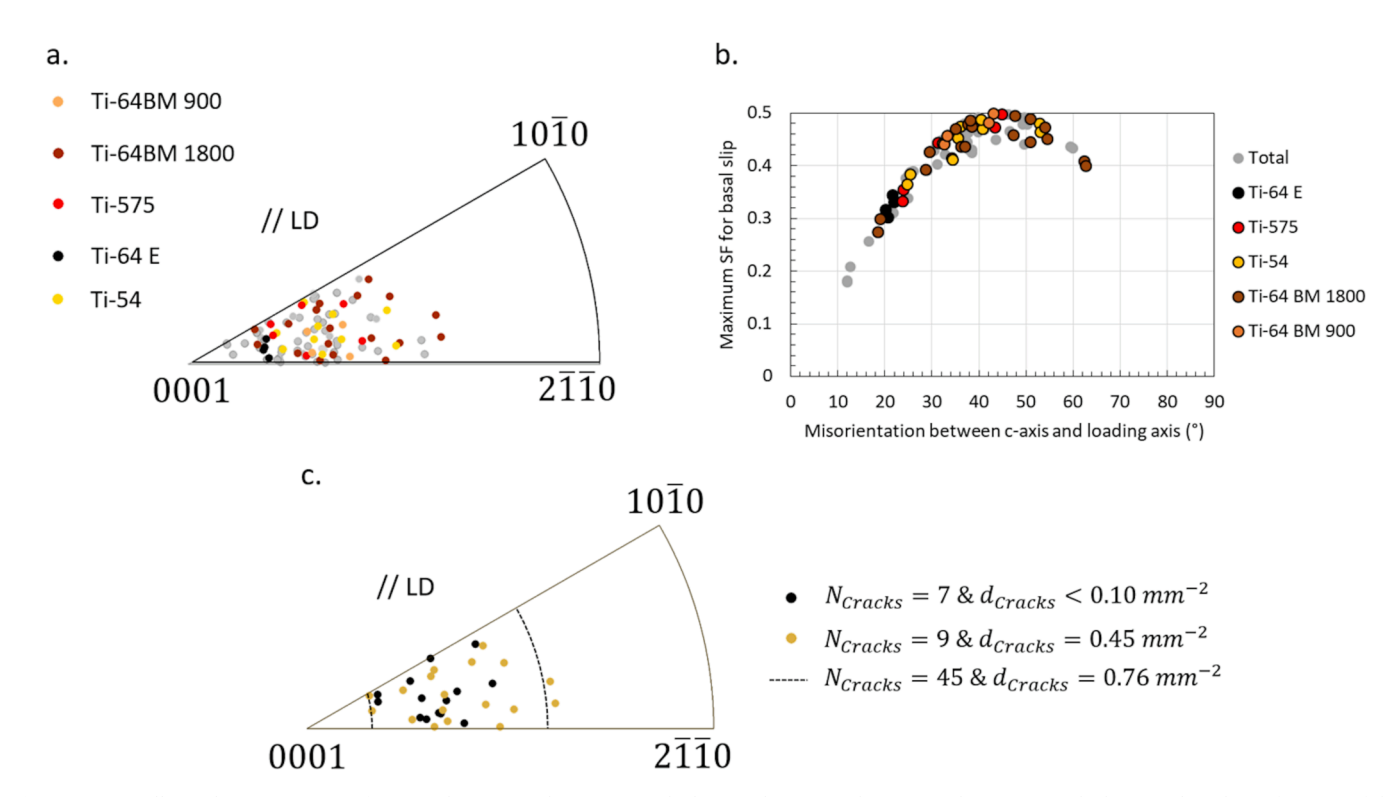


Fig. 6. a. Crystallographic orientations of equiaxed α grains adjacent to cracked BTGB, b. Equiaxed α grains adjacent to cracked BTGB plotted as a function of the maximum Schmid factor for basal slip and the misorientation between the c-axis of the HCP lattice and the loading axis, and c. Crystallographic orientations of equiaxed α grains adjacent to cracked BTGB in Ti-64BM, suggesting that the orientation domain extends with increasing crack densities (d_{Cracks}). Crystallographic orientations in Fig. 6a and 6c are given along the loading direction (LD).

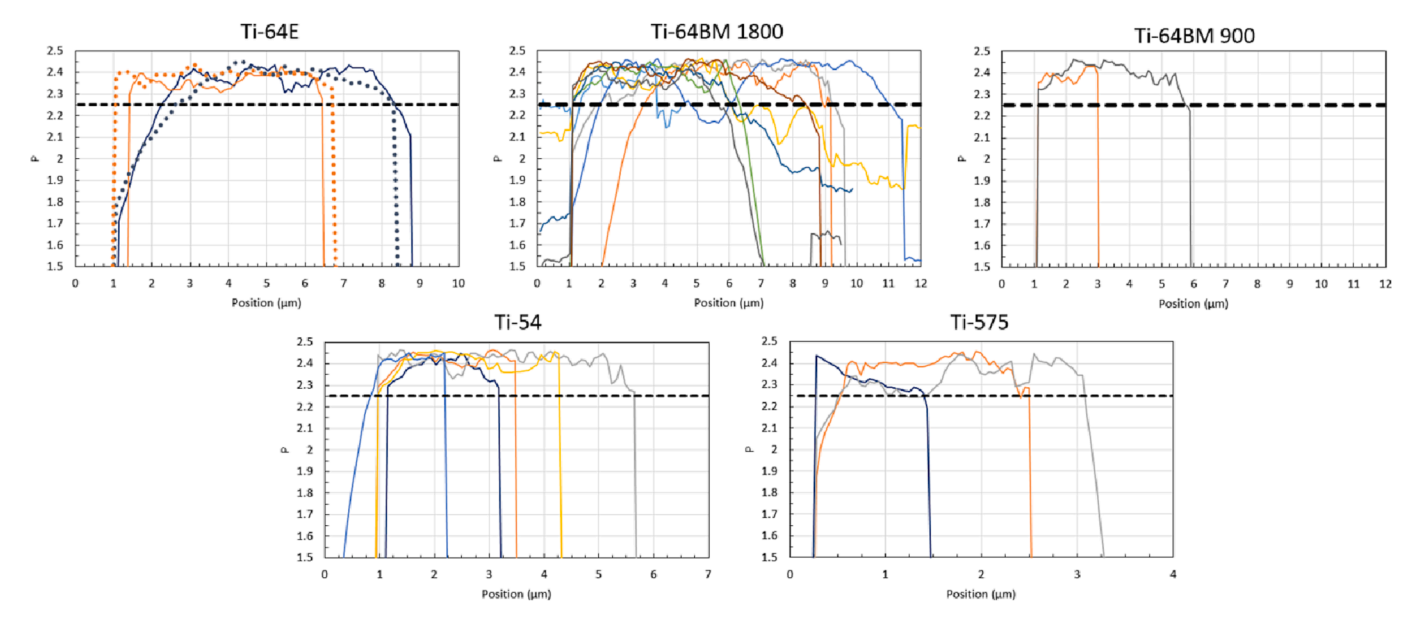


Fig. 7. Profiles of P values along cracked BTGB in the different specimens tested.

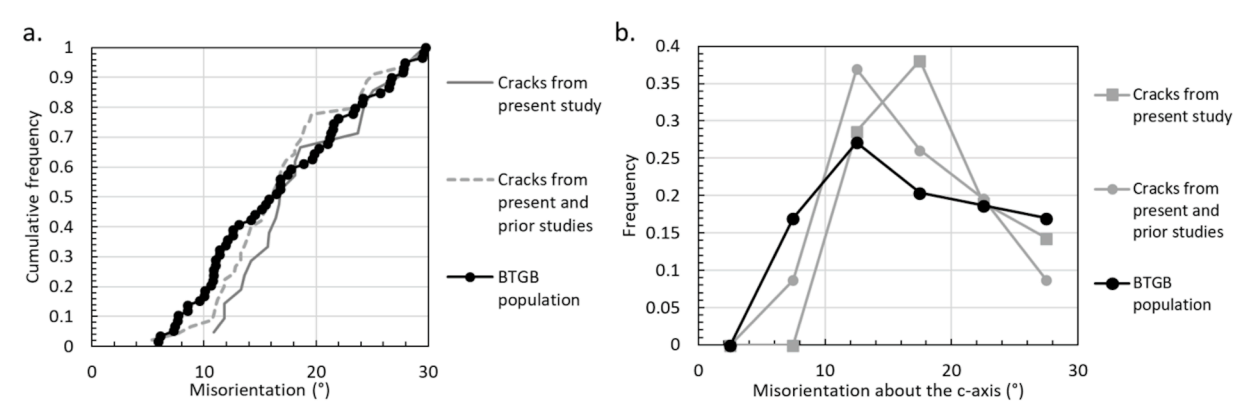


Fig. 8. a. Cumulative distribution plot of misorientation values measured experimentally either between cracked BTGB or between BTGB identified using the presently reported detection routine, b. Distribution of values plotted using 5° bins.

a maximum Schmid factor for basal slip higher than 0.2. This partitioning step is illustrated in Fig. 9. The subsequent application of criteria presented in previous paragraphs results in the successful detection of the crack contained in this region. In the 15 $\,\mathrm{mm}^2$ region, 71 BTGB segments are candidates for crack initiation. Thus, the associated density is approximately 4.7 $\,\mathrm{mm}^{-2}.$

The binary image containing BTGB segments being candidates for crack initiation was processed to study their spatial distribution. 1000 randomly positioned samples with subset sizes ranging from 1 μm to 1250 μm were randomly positioned within the 3×5 mm^2 region. The probability of finding at least one candidate for crack initiation is plotted in Fig. 10 as a function of the subset size. The probability exceeds 95 % for considered areas higher than $790\times790~\mu m^2$ (88 times the average α grain size). Areas higher than $1090\times1090~\mu m^2$ (121 times the average α grain size) must be considered to contain at least one candidate for crack initiation. The corresponding areas account for approximately 24 and 13 times the area of the EBSD map, which can then be considered representative.

4. Discussion

4.1. Influence of composition and microstructure

Microstructural statistics were collected on different Ti-Al-V based

alloys with various microstructures. Tests in the LCF regime were interrupted early to extract the most critical microstructural configurations for crack nucleation. Importantly, all cracks were located at BTGB regardless of the alloy composition and microstructure. Employed materials exhibit a different balance in α and β stabilizers due to the various Al and V contents. It leads to differences in α grain size, β phase fraction, and composition in equiaxed α grains, which have not noticeably influenced the cracking sensitivity of BTGB. The comparison of metrics related to the grain boundary or crystallographic orientations of adjacent grains with data from prior studies [6,17,18] revealed no significant difference. This shows that i. the collected dataset is statistically meaningful and ii. early crack formation at BTGB is a general mechanism in near- α and $\alpha + \beta$ Ti alloys. Finally, the presence of lamellar α phase in Ti-64 and Ti-575 with similar transformed β area fractions, while likely to change the stress and strain partitioning among microstructural constituents, did not change the cracking mechanism either. The set of composition, microstructural parameters, and loading conditions considered in this study and prior investigations showing crack initiation along BTGB is summarized in Fig. 11 [6,17,18]. A single criterion can then be established to detect crack initiation sites for various materials.

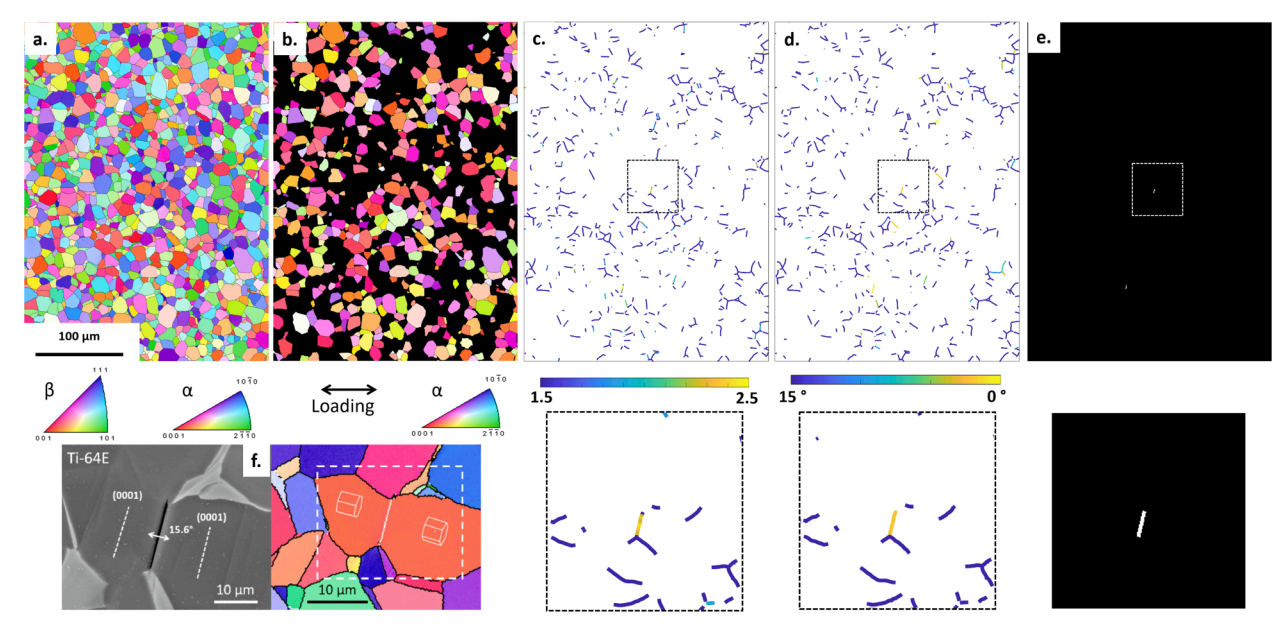


Fig. 9. Images illustrating the sequential processes involving partitioning of EBSD data (a. and b.), calculation of P values along α/α grain boundaries (c.), calculation of misorientation between c-axes (d), and segmentation of BTGB according to crystallographic, length and P value based criteria. SEM and EBSD maps showing the crack are also indicated (f.). Crystallographic orientations are along the loading direction, which is horizontal.

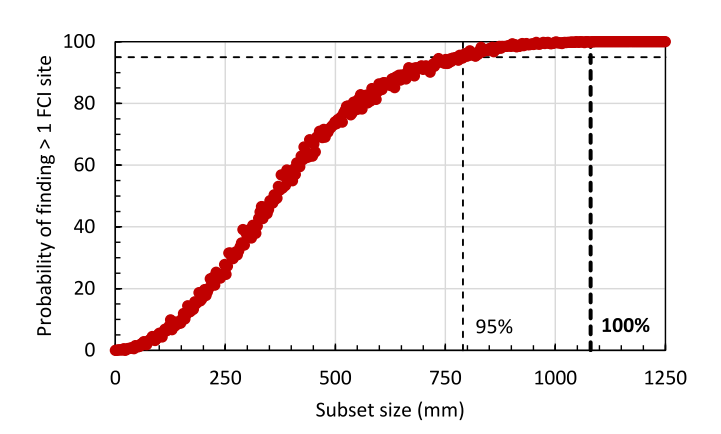


Fig. 10. Probability of finding at least one potential fatigue crack initiation site (FCI) as a function of the subset size. Size thresholds to exceed 95 % or reach 100 % are indicated.

4.2. Microstructural statistics

Numerous metrics were considered to identify microstructural configurations prone to early LCF crack nucleation. A set of criteria was then established based on the collected data. C-axes are well aligned across cracked BTGB, with a misorientation lower than $4^\circ.$ This value is likely overestimated due to lattice rotation imposed by crack opening (i.e., typically about 1° [18]). Cracked BTGB most frequently display a $10^\circ-20^\circ$ misorientation, although other values in the $5^\circ-30^\circ$ range were also often found. No specific misorientation angle about the c-axis is associated with cracking, and the obtained trends reflect the overall distribution of misorientation values measured across BTGB.

The crystallographic orientation of α grains adjacent to cracked BTGB was also a valuable indicator to identify potential crack initiation sites. All c-axes were misaligned from the loading axis by more than 10° and less than 65° . Extension of the orientation domain was suggested upon nucleation of a greater number of cracks, which implies cracking of less favorable configurations. This feature was highlighted considering different tests on the same material and continued until different crack densities. BTGB with lower magnitudes of resolved shear stress and/or

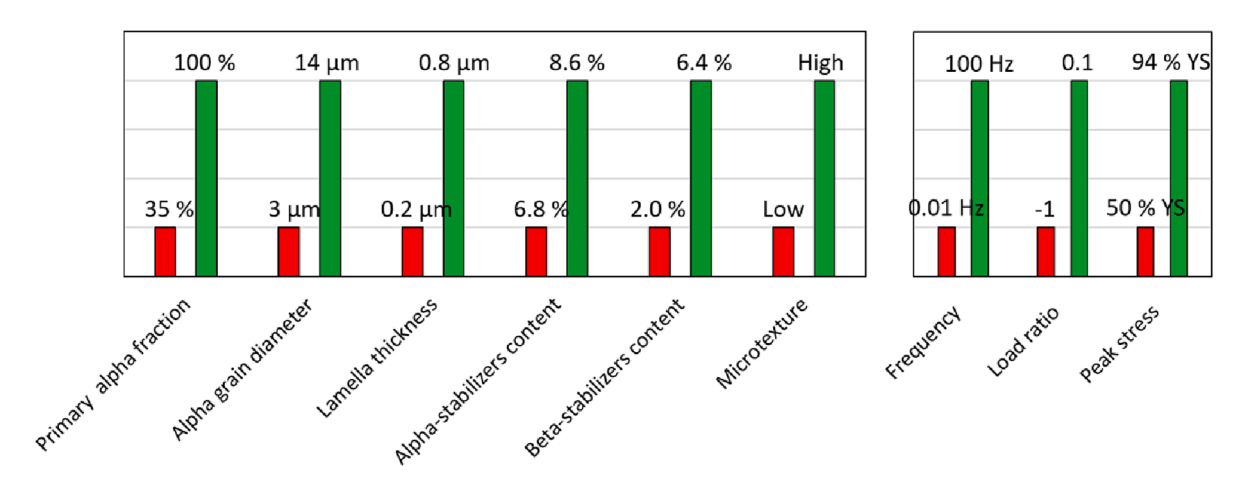


Fig. 11. Bar chart showing the range of microstructural and loading parameters leading to fatigue crack nucleation at BTGB. Alpha and beta-stabilizers content are given in Al and Mo equivalent concentrations [39].

stress component normal to the basal planes then require more cycles to crack. This feature highlights the importance of mechanical considerations to refine the prediction of the most critical configurations.

The length of the BTGB segment connected to the specimen surface appears of little importance in identifying the most critical configuration. However, cracks were found on BTGB segments longer than 40 % of the average α grain size, unless slip transfer allowed the effective slip length to be locally higher. Therefore, microtextured regions are likely promoting BTGB cracking and increased densities of candidates to crack nucleation due to the easier slip transfer [40,41]. In addition, it was observed that the crack path deviates from the pre-existing slip bands during crack extension beyond the initiation BTGB. It highlights a particular role of BTGB in driving crack growth along an easy path, and that fatigue crack growth does not occur along pre-existing slip bands. Prior studies have highlighted that crack initiation can proceed along basal planes, while growth occurs along near-basal planes [5,14]. Based on the presently reported observations, one can infer that this specific behavior is possibly due to the presence of BTGB at the crack nucleation site.

4.3. Densities of BTGB and potential fatigue crack initiation sites

BTGB detection was successfully achieved using an automatic processing routine. An estimation of the BTGB density could then be assessed. 7.8 occurrences were found on average in a square millimeter, which contains approximately 16.6×10^3 equiaxed α grains. However, this value should be taken with care. Conventional EBSD mapping does not provide complete 3D information about the α/α grain boundary plane. With this approach, some grain boundaries might be wrongly classified as BTGB in the case the GB trace is parallel to basal plane traces, while the three planes are not parallel. In addition, EBSD mapping does not provide a perfect description of microstructure because artifacts such as beam drift, distortions, spatial sampling (i.e., step size), and noise (i.e., misindexed points), may impair the description of the grain boundary trace. Therefore, the density of BTGB and fatigue crack initiation sites should not be considered as 100 % accurate, although it provides quantitative estimates and reliable orders of magnitudes. Large scale 3D analyses might be carried out on carefully reconstructed microstructures for more accurate assessments [42,43].

Based on the processing routine for BTGB detection and the statistical analysis of fatigue crack initiation sites, specific criteria were implemented to identify candidates for crack initiation in a large scale EBSD map. The resulting density of candidates for crack initiation is about 4.7 mm⁻². Areas greater than 1 mm², and 100 times the average α grain size, have then to be considered to include at least one BTGB susceptible to cracking in the region of interest. As compared to Ni-based superalloys, which have been the subject of similar analysis, a far lower density of potential crack initiation sites is available [34]. The minimum subset size to include at least one potential crack initiation site was estimated to be about 4.2 or 9.2 times the grain size for René 88DT and IN100, respectively, versus 121 times the α grain size in Ti-64E. With subset sizes of 396 \times 396 μm^2 and 110 \times 110 μm^2 for IN100 and René 88DT, respectively, the minimum subset size to include at least one potential crack initiation site is roughly 2 to 10 times larger for Ti alloys. This feature is likely related to the high variability in fatigue life reported for Ti alloys. It implies the usage of high-resolution characterization over large regions to ensure representativity of investigations focused on fatigue crack initiation in Ti alloys. Indeed, mechanical constraints imposed by microstructural neighborhood [12,44,45], and the crack growth behavior [5,16,46,47], also significantly contribute to the total fatigue life. A representative volume element regarding the life to crack nucleation, or the total fatigue life, should then contain many candidates for fatigue crack nucleation to capture the most critical configuration.

5. Conclusion

Low-cycle fatigue crack initiation was investigated in different alloys with Ti-Al-V based compositions and various microstructures. Microstructural configurations at crack initiation sites were analyzed to highlight critical characteristics. Based on this information, an automated processing routine was developed to identify candidates for fatigue crack nucleation. Most salient conclusions can be drawn as follows:

- Recently developed Ti-54 and Ti-575 alloys are prone to early LCF crack formation at BTGB in the same way as Ti-64. The analysis of microstructural features at crack nucleation sites suggested that the crack initiation mechanism is not sensitive to the α grain size, the primary α fraction, and the Al/V content in the investigated ranges.
- Crack nucleation and growth along the BTGB separating the initiation α grain pair leads to facets parallel to basal planes. The crack path then appears constrained along the BTGB, possibly due to lower cleavage energy as compared to transgranular cracking. Away from the BTGB, growth proceeds slightly off basal planes. Crack tip stress state and plasticity become more important to determine the crack path, as cracks were not found to grow along pre-existing slip bands.
- Early cracking of BTGB appeared weakly sensitive to the misorientation about the c-axis, as its distribution is similar to the population of BTGB in the material. Also, the length of the grain boundary segment on the surface of the specimen is not critical, as slip transmission seemingly allows crack formation along short BTGB segments. The extension of the crystallographic orientation domain of α grains associated with crack initiation suggests that the local mechanical state is important to determine the most critical microstructure configurations.
- A procedure was proposed to detect BTGB and microstructural configurations candidates to crack initiation based on a statistically significant number of observations. The BTGB density in the reference material used in this study is about 7.8 mm $^{-2}$. Considering additional criteria to identify potential crack nucleation sites, the density of BTGB susceptible to cracking is about 4.7 mm $^{-2}$. The minimum area to consider to include a potential crack initiation site is approximately 1.1×1.1 mm 2 (i.e., roughly 120 times the average α grain size). This feature is likely related to the high variability in fatigue life reported for Ti alloys, as these values are higher than for other metallic materials.

CRediT authorship contribution statement

C. Bean: Investigation, Writing – review & editing. J.C. Stinville: Investigation, Methodology, Supervision, Writing – review & editing. A. Naït-Ali: Investigation. Z. Wu: Resources, Writing – review & editing. F. Sun: Resources, Writing – review & editing. F. Prima: Resources, Writing – review & editing. S. Hemery: Conceptualization, Methodology, Investigation, Resources, Writing – original draft.

Declaration of Competing Interest

The authors declare that they have no known competing financial interests or personal relationships that could have appeared to influence the work reported in this paper.

Data availability

Data will be made available on request.

Acknowledgement

This work has been partially supported by « Nouvelle Aquitaine » Region and by European Structural and Investment Funds (ERDF reference: P-2016-BAFE-94/95). Institut Pprime gratefully

acknowledges "Contrat de Plan Etat - Région Nouvelle-Aquitaine" (CPER) as well as the "Fonds Européen de Développement Régional (FEDER)" for their financial support to the reported work. CB and JCS are grateful for financial support from the Energy & Biosciences Institute (EBI), USA through the EBI-Shell Program and the NSF (award #2234892). Marie-Agathe Charpagne is acknowledged for fruitful discussions. Tresa M. Pollock is acknowledged for providing the Ti-64E material.

References

- [1] Golden PJ, John R, Porter WJ. Variability in room temperature fatigue life of alpha +beta processed Ti-6Al-4V. Int J Fatigue 2009;31:1764-70. https://doi.org/ 10.1016/j.ijfatigue.2009.01.005.
- [2] Jha SK, Szczepanski CJ, Golden PJ, Porter WJ, John R. Characterization of fatigue crack-initiation facets in relation to lifetime variability in Ti-6Al-4V. Int J Fatigue 2012;42:248-57. https://doi.org/10.1016/j.ijfatigue.2011.11.017.
- [3] Prasad K, Sarkar R, Singh V, Ghosal P, Bhattacharjee A, Gokhale H. On the probabilistic assessment of variability in fatigue life in a near α titanium alloy Timetal 834: Crystallography of fatigue crack initiating facets. Acta Mater 2021; 218:117214. https://doi.org/10.1016/j.actamat.2021.117214.
- [4] Szczepanski CJ, Jha SK, Larsen JM, Jones JW. Microstructural Influences on Very-High-Cycle Fatigue-Crack Initiation in Ti-6246. Metall Mater Trans A 2008;39: 2841–51. https://doi.org/10.1007/s11661-008-9633-z.
- [5] Sinha V, Pilchak AL, Jha SK, Porter WJ, John R, Larsen JM. Correlating Scatter in Fatigue Life with Fracture Mechanisms in Forged Ti-6242Si Alloy. Metall Mater Trans A 2018;49:1061–78. https://doi.org/10.1007/s11661-017-4437-7.
- [6] Lavogiez C, Dureau C, Nadot Y, Villechaise P, Hémery S. Crack initiation mechanisms in Ti-6Al-4V subjected to cold dwell-fatigue, low-cycle fatigue and high-cycle fatigue loadings. Acta Mater 2023;244:118560. https://doi.org/ 10.1016/j.actamat.2022.118560.
- [7] Ravi Chandran KS, Jha SK. Duality of the S-N fatigue curve caused by competing failure modes in a titanium alloy and the role of Poisson defect statistics. Acta Mater 2005;53:1867–81. https://doi.org/10.1016/j.actamat.2004.12.032.
- [8] Bridier F, Villechaise P, Mendez J. Slip and fatigue crack formation processes in an α/β titanium alloy in relation to crystallographic texture on different scales. Acta Mater 2008;56:3951–62. https://doi.org/10.1016/j.actamat.2008.04.036.
- [9] Jha SK, Szczepanski CJ, John R, Larsen JM. Deformation heterogeneities and their role in life-limiting fatigue failures in a two-phase titanium alloy. Acta Mater 2015; 82:378–95. https://doi.org/10.1016/j.actamat.2014.08.034.
- [10] Przybyla CP, McDowell DL. Simulated microstructure-sensitive extreme value probabilities for high cycle fatigue of duplex Ti-6Al-4V. Int J Plast 2011;27: 1871-95. https://doi.org/10.1016/j.ijplas.2011.01.006.
- [11] Lucarini S, Segurado J. An upscaling approach for micromechanics based fatigue: from RVEs to specimens and component life prediction. Int J Fract 2020;223: 93–108. https://doi.org/10.1007/s10704-019-00406-5.
- [12] Gu T, Stopka K, Xu C, McDowell D. Modeling the Statistical Distribution of Fatigue Crack Formation Lifetime in Large Volumes of Polycrystalline Microstructures. Acta Mater 2023:118715. https://doi.org/10.1016/j.actamat.2023.118715.
- [13] Shen J, Kotha S, Noraas R, Venkatesh V, Ghosh S. Developing parametrically upscaled constitutive and crack nucleation models for the α/β Ti64 alloy. Int J Plast 2022;151:103182. https://doi.org/10.1016/j.ijplas.2021.103182.
- [14] Pilchak AL, Williams JC. Observations of Facet Formation in Near-α Titanium and Comments on the Role of Hydrogen. Metall Mater Trans A 2011;42:1000–27. https://doi.org/10.1007/s11661-010-0507-9.
- [15] Tympel PO, Lindley TC, Saunders EA, Dixon M, Dye D. Influence of complex LCF and dwell load regimes on fatigue of Ti-6Al-4V. Acta Mater 2016;103:77–88. https://doi.org/10.1016/j.actamat.2015.09.014.
- [16] Bantounas I, Dye D, Lindley TC. The effect of grain orientation on fracture morphology during high-cycle fatigue of Ti-6Al-4V. Acta Mater 2009;57:3584-95. https://doi.org/10.1016/j.actamat.2009.04.018.
- [17] Lavogiez C, Hémery S, Villechaise P. On the mechanism of fatigue and dwell-fatigue crack initiation in Ti-6Al-4V. Scr Mater 2020;183:117–21. https://doi.org/10.1016/j.scriptamat.2020.03.031.
- [18] Hémery S, Stinville JC, Wang F, Charpagne MA, Emigh MG, Pollock TM, et al. Strain localization and fatigue crack formation at (0001) twist boundaries in titanium alloys. Acta Mater 2021;219:117227. https://doi.org/10.1016/j. actamat 2021 117227
- [19] Wu Z, Kou H, Li J, Hémery S, Chen N, Tang J, et al. High-strength and low-dwell-sensitivity titanium alloy showing high tolerance to microcracking under dwell fatigue condition. Int J Plast 2022;159:103449. https://doi.org/10.1016/j.iiplas.2022.103449.
- [20] Liu C, Thomas R, Sun T, Donoghue J, Zhang X, Burnett TL, et al. Multi-dimensional study of the effect of early slip activity on fatigue crack initiation in a near-a titanium alloy. Acta Mater 2022:117967. https://doi.org/10.1016/j. actamat.2022.117967.
- [21] Fan J, Zhang W, Li B, Li K, Wang Y, Jiang P, et al. Crystallographic analysis of slip system activation in bimodal Ti–6Al–3Nb–2Zr–1Mo alloy under various dwellfatigue loadings. Mater Sci Eng A 2023:144610. https://doi.org/10.1016/j. msea.2023.144610.
- [22] Liu C, Xu X, Sun T, Thomas R, da Fonseca JQ, Preuss M. Microstructural effects on fatigue crack initiation mechanisms in a near-alpha titanium alloy. Acta Mater 2023;253:118957. https://doi.org/10.1016/j.actamat.2023.118957.

- [23] Bouchedjra M, Kanit T, Boulemia C, Amrouche A, Belouchrani MEA. Determination of the RVE size for polycrystal metals to predict monotonic and cyclic elastoplastic behavior: Statistical and numerical approach with new criteria. Eur J Mech A Solids 2018;72:1–15. https://doi.org/10.1016/j.euromechsol.2018.04.011.
- [24] Kanit T, Forest S, Galliet I, Mounoury V, Jeulin D. Determination of the size of the representative volume element for random composites: statistical and numerical approach. Int J Solids Struct 2003;40:3647–79. https://doi.org/10.1016/S0020-7683(03)00143-4
- [25] Yang S, Dirrenberger J, Monteiro E, Ranc N. Representative volume element size determination for viscoplastic properties in polycrystalline materials. Int J Solids Struct 2019;158:210–9. https://doi.org/10.1016/j.ijsolstr.2018.09.011.
- [26] Vieira RB, Sehitoglu H, Lambros J. Representative volume elements for plasticity and creep measured from high-resolution microscale strain fields. Acta Mater 2021;214:117021. https://doi.org/10.1016/j.actamat.2021.117021.
- [27] Efstathiou C, Sehitoglu H, Lambros J. Multiscale strain measurements of plastically deforming polycrystalline titanium: Role of deformation heterogeneities. Int J Plast 2010;26:93–106. https://doi.org/10.1016/j.ijplas.2009.04.006.
- [28] Chatterjee K, Echlin MP, Kasemer M, Callahan PG, Pollock TM, Dawson P. Prediction of tensile stiffness and strength of Ti-6Al-4V using instantiated volume elements and crystal plasticity. Acta Mater 2018;157:21–32. https://doi.org/ 10.1016/j.actamat.2018.07.011.
- [29] Echlin MP, Kasemer M, Chatterjee K, Boyce D, Stinville JC, Callahan PG, et al. Microstructure-Based Estimation of Strength and Ductility Distributions for α+β Titanium Alloys. Metall Mater Trans A 2021;52:2411–34. https://doi.org/ 10.1007/s11661-021-06233-5.
- [30] Sangid MD, Rotella J, Naragani D, Park J-S, Kenesei P, Shade PA. A complete grain-level assessment of the stress-strain evolution and associated deformation response in polycrystalline alloys. Acta Mater 2020;201:36–54. https://doi.org/10.1016/j.actamat.2020.09.051.
- [31] Rotella J, Pilchak AL, Sangid MD. Examining the pathways for deformation band formation at the mesoscale. Mater Charact 2021;182:111552. https://doi.org/ 10.1016/j.matchar.2021.111552.
- [32] Stinville JC, Charpagne MA, Cervellon A, Hemery S, Wang F, Callahan PG, et al. On the origins of fatigue strength in crystalline metallic materials. Science 2022;377: 1065–71. https://doi.org/10.1126/science.abn0392.
- [33] Gillner K, Münstermann S. Numerically predicted high cycle fatigue properties through representative volume elements of the microstructure. Int J Fatigue 2017; 105:219–34. https://doi.org/10.1016/j.jifatigue.2017.09.002.
- [34] Stinville JC, Lenthe WC, Echlin MP, Callahan PG, Texier D, Pollock TM. Microstructural statistics for fatigue crack initiation in polycrystalline nickel-base superalloys. Int J Fract 2017;208:221–40. https://doi.org/10.1007/s10704-017-0241-z.
- [35] Segurado J, Lebensohn RA, LLorca J. Chapter One Computational Homogenization of Polycrystals. In: Hussein, MI, editor. Advances in Applied Mechanics. Elsevier; 2018, pp. 1–114. https://doi.org/10.1016/bs. aams.2018.07.001.
- [36] Bagri A, Weber G, Stinville J-C, Lenthe W, Pollock T, Woodward C, et al. Microstructure and Property-Based Statistically Equivalent Representative Volume Elements for Polycrystalline Ni-Based Superalloys Containing Annealing Twins. Metall Mater Trans A 2018;49:5727–44. https://doi.org/10.1007/s11661-018-4858-y.
- [37] Semiatin SL, Kirby BC, Salishchev GA. Coarsening behavior of an alpha-beta titanium alloy. Metall Mater Trans A 2004;35:2809–19. https://doi.org/10.1007/ s11661-004-0228-z.
- [38] Bachmann F, Hielscher R, Schaeben H. Texture Analysis with MTEX Free and Open Source Software Toolbox. Solid State Phenom 2010;160:63–8. https://doi. org/10.4028/www.scientific.net/SSP.160.63.
- [39] Litifering G, Williams JC. Titanium. Berlin, Heidelberg: Springer; 2007. https://www.springer.com/gp/book/9783540713975 (accessed September 10, 2020.
- [40] Hémery S, Nizou P, Villechaise P. In situ SEM investigation of slip transfer in Ti-6Al-4V: Effect of applied stress. Mater Sci Eng A 2018;709:277–84. https://doi.org/10.1016/j.msea.2017.10.058.
- [41] Echlin MP, Stinville JC, Miller VM, Lenthe WC, Pollock TM. Incipient slip and long range plastic strain localization in microtextured Ti-6Al-4V titanium. Acta Mater 2016;114:164–75. https://doi.org/10.1016/j.actamat.2016.04.057.
- [42] Echlin MP, Straw M, Randolph S, Filevich J, Pollock TM. The TriBeam system: Femtosecond laser ablation in situ SEM. Mater Charact 2015;100:1–12. https://doi.org/10.1016/j.matchar.2014.10.023.
- [43] DeMott R, Collins P, Kong C, Liao X, Ringer S, Primig S. 3D electron backscatter diffraction study of α lath morphology in additively manufactured Ti-6Al-4V. Ultramicroscopy 2020;218:113073. https://doi.org/10.1016/j. ultramic 2020 113073
- [44] Stopka KS, Yaghoobi M, Allison JE, McDowell DL. Simulated effects of sample size and grain neighborhood on the modeling of extreme value fatigue response. Acta Mater 2022;224:117524. https://doi.org/10.1016/j.actamat.2021.117524.
- [45] McDowell DL, Dunne FPE. Microstructure-sensitive computational modeling of fatigue crack formation. Int J Fatigue 2010;32:1521–42. https://doi.org/10.1016/ j.ijfatigue.2010.01.003.
- [46] Hémery S, Stinville JC. Microstructural and load hold effects on small fatigue crack growth in α+β dual phase Ti alloys. Int J Fatigue 2022;156:106699. https://doi. org/10.1016/j.ijfatigue.2021.106699.
- [47] Zhang K, Wu X, Davies CHJ. Effect of microtexture on short crack propagation in two-phase titanium alloys. Int J Fatigue 2017;104:206–20. https://doi.org/ 10.1016/j.ijfatigue.2017.07.022.